Supplementary Information: Topological superconductivity in a designer ferromagnet-superconductor van der Waals heterostructure

Shawulienu Kezilebieke,[1,*] Md Nurul Huda,[1] Viliam Vaňo,[1] Markus Aapro,[1] Somesh C. Ganguli,[1] Orlando J. Silveira,[1] Szczepan Głodzik,[2] Adam S. Foster,[1,3] Teemu Ojanen,[4,5,*] and Peter Liljeroth[1,*]

[1] *Department of Applied Physics, Aalto University School of Science, PO Box 15100, 00076 Aalto, Finland*

[2] *Institute of Physics, M. Curie-Skłodowska University, 20-031 Lublin, Poland*

[3] *WPI Nano Life Science Institute (WPI-NanoLSI), Kanazawa University, Kakuma-machi, Kanazawa 920-1192, Japan*

[4] *Computational Physics Laboratory, Physics Unit, Faculty of Engineering and Natural, Sciences, Tampere University, PO Box 692, FI-33014 Tampere, Finland*

[5] *Helsinki Institute of Physics PO Box 64, FI-00014, Finland*

1. THEORETICAL DESCRIPTION

Here we establish a phenomenological model of 2H-$NbSe_2$ covered by a magnetic insulator and provide a theoretical description of topological superconductivity in this system. Bulk 2H-$NbSe_2$ has a quasi-2D layered structure consisting of stacked units of Nb atoms on a triangular lattice sandwiched between Se layers. The detailed microscopic description of heterostructures with magnetic $CrBr_3$ on superconducting $NbSe_2$ becomes quickly unmanageable, thus we formulate an effective low-energy theory with appropriate symmetries, supplemented by information from the DFT calculations. The nature of topological superconductivity can be understood from the lattice and discrete symmetries that are insensitive to model details. Thus, it is sufficient to devise a minimum model that displays the essential features of the real structure. The bands near the Fermi energy mostly derive from Nb d-orbitals and the relevant low-energy physics can be qualitatively reproduced by a minimum model with one effective d orbital per site on a triangular lattice. This approximation treats the system effectively as a 2D structure, neglecting the bands exhibiting strong k_z dispersion and the less important Se-derived three-dimensional bands near the Γ point. Experimental observations of magnetic impurities in bulk 2H-$NbSe_2$ highlight the 2D nature of the magnetically-induced subgap states and the qualitative validity of treating the layers as effectively decoupled[1]. Thus, the experimental evidence suggests that our model captures the qualitative behaviour of the top layer in contact with the magnet in multilayer systems. Furthermore, chiral topological superconductivity discussed here is effectively a two-dimensional phenomenon which motivates the two-dimensional description with $k_z = 0$. The studied Hamiltonian defined on a triangular lattice thus becomes $\hat{H} = \hat{H}_t + \hat{H}_{SOC} + \hat{H}_M + \hat{H}_{SC}$, where:

$$
\begin{aligned}
\hat{H}_t &= -\sum_{\mathbf{i},\mathbf{j},\sigma} t_{\mathbf{ij}} c^\dagger_{\mathbf{i}\sigma} c_{\mathbf{j}\sigma} - \mu \sum_{\mathbf{i},\sigma} c^\dagger_{\mathbf{i}\sigma} c_{\mathbf{i}\sigma} \\
\hat{H}_{SOC} &= i\alpha_R \sum_{\langle \mathbf{i},\mathbf{j}\rangle,\sigma,\sigma'} [\boldsymbol{e}_z \cdot \boldsymbol{e}_{\mathbf{ij}} \times \boldsymbol{\sigma}]^{\sigma\sigma'} c^\dagger_{\mathbf{i}\sigma} c_{\mathbf{j}\sigma'} - i\lambda \sum_{\langle \mathbf{i},\mathbf{j}\rangle,\sigma,\sigma'} e^{3i\theta_{\mathbf{ij}}} \sigma_z^{\sigma\sigma'} c^\dagger_{\mathbf{i}\sigma} c_{\mathbf{j}\sigma'}, \\
\hat{H}_M &= -\sum_{\mathbf{i},\sigma,\sigma'} \big([\mathbf{V_Z}(\mathbf{i})\cdot]_{\sigma,\sigma'} + V_S \delta_{\sigma,\sigma'}\big) c^\dagger_{\mathbf{i}\sigma} c_{\mathbf{i}\sigma'}, \\
\hat{H}_{SC} &= \sum_{\mathbf{i}} \Delta (c^\dagger_{\mathbf{i}\uparrow} c^\dagger_{\mathbf{i}\downarrow} + H.c.).
\end{aligned}
\tag{1}
$$

The symbol $t_{\mathbf{ij}}$ corresponds to the hopping amplitudes and μ is the chemical potential. The spin-orbit coupling (SOC) consists of an in-plane Rashba contribution with strength α_R and the out-of-plane Ising-type with strength λ. The Rashba term is orthogonal to the bond vectors $\boldsymbol{e}_{\mathbf{ij}}$ and the Ising SOC is determined by $\theta_{\mathbf{ij}}$ which stands for the angle the vector connecting $\mathbf{i}$ and $\mathbf{j}$ sites makes with the positive x axis (so that $e^{3i\theta_{\mathbf{ij}}} = \pm 1$). The vector of the Pauli matrices representing spin is denoted by σ. The coordinate system is chosen so that the x axis coincides with one of the lattice vectors. It should be emphasized that the values of spin-orbit couplings (as well as other parameters) are specific to the studied heterostructure and not the bulk materials. Especially the Rashba coupling is expected to be completely determined by the interface and not the properties of $CrBr_3$ or $NbSe_2$ alone. The magnetic material gives rise to a Zeeman splitting $\mathbf{V_Z}$ and a scalar potential V_S and Δ describes the superconducting pairing. Pauli matrices σ act on the spin degrees of freedom. To model the experimental system, magnetization is chosen to point in the z direction $\mathbf{V_Z} = [0, 0, V_Z]$.

The system is most conveniently analyzed by assuming translational symmetry, passing to momentum space and working in the Nambu basis $\psi = (c_{k\uparrow}, c_{k\downarrow}, c^\dagger_{k\downarrow}, -c^\dagger_{k\uparrow})^T$ where the Bogoliubov-de Gennes (BdG) Hamiltonian becomes

$$H = E_t(k)\tau_z + E_{R_x}(k)\tau_z\sigma_x + E_{R_y}(k)\tau_z\sigma_y + E_I(k)\tau_z\sigma_z + V_Z\sigma_z + \Delta\tau_x. \tag{2}$$

Here we have introduced additional Pauli matrices τ_i that operate in the particle-hole space so the resulting expression has a 4×4 matrix structure. The SOC terms are given by

$$\begin{aligned} E_{R_x}(k) &= 2\alpha_R\sqrt{3}\sin(\tfrac{k_y a\sqrt{3}}{2})\cos(\tfrac{k_x a}{2}), \\ E_{R_y}(k) &= -2\alpha_R\big(\sin(k_x a) + \sin(\tfrac{k_x a}{2})\cos(\tfrac{k_y a\sqrt{3}}{2})\big), \end{aligned}$$

and

$$E_I(k) = 2\lambda\Big[\sin\big(k_x a\big) - \sin\big(\tfrac{k_x a}{2} - \tfrac{k_y\sqrt{3}a}{2}\big) - \sin\big(\tfrac{k_x a}{2} + \tfrac{k_y\sqrt{3}a}{2}\big)\Big]. \tag{3}$$

For selected purposes below, we consider a simple third-neighbour hopping form for the normal band structure $E_t(k) = \epsilon(k) - \mu + V_S$ with

$$\begin{aligned} \epsilon(k) = &-2t_1\Big[\cos\big(k_x a\big) + 2\cos\big(\tfrac{k_x a}{2}\big)\cos\big(\tfrac{k_y a\sqrt{3}}{2}\big)\Big] - 2t_2\Big[\cos\big(k_y\sqrt{3}a\big) + 2\cos\big(\tfrac{k_x 3a}{2}\big)\cos\big(\tfrac{k_y\sqrt{3}a}{2}\big)\Big] \\ &- 2t_3\Big[\cos\big(2k_x a\big) + 2\cos\big(k_x a\big)\cos\big(k_y\sqrt{3}a\big)\Big]. \end{aligned} \tag{4}$$

This form of $\epsilon(k)$ with parameters $t_1 = -0.04$, $t_2 = -0.132$, $t_3 = -0.012$, $\mu = -0.260$ (in the units of eV) captures the generic features of the quasi-2D d-band in 2H-$NbSe_2$ from the band bottom up to ~ 0.4 eV as shown in Supplementary Fig. 1. However, it should be kept in mind that the following expressions for the spectrum of the system and conditions for the existence of topological phases hold for general $E_t(k)$. It is expected that the presence of the magnetic material substantially modifies the properties of the underlying system, and it is reasonable to expect that $E_t(k)$ deviates from the known bulk band structure of $NbSe_2$. Thus, in the effective theory it is not meaningful to attempt more thorough fitting to the $NbSe_2$ band structure in the absence of $CrBr_3$.

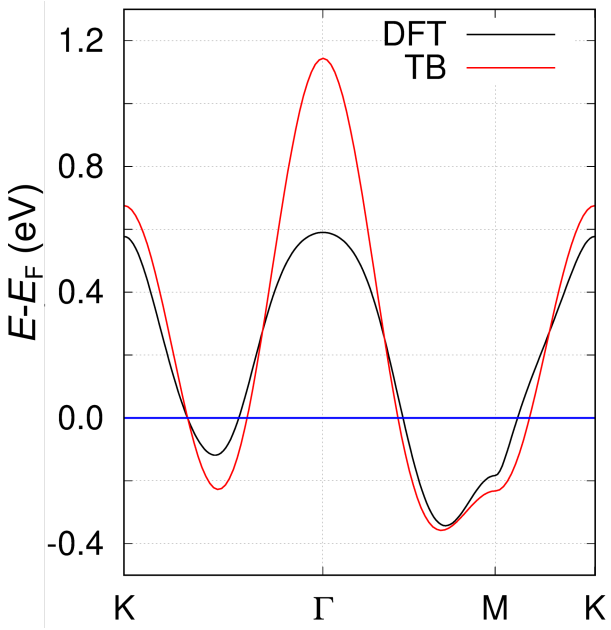

Supplementary Figure 1. Comparison of the DFT and the 3rd neighbour tight-binding approximation results for the quasi-2D $NbSe_2$ d band without spin-orbit effects.

The BdG Hamiltonian has two positive and two negative energy branches. In the absence of the Ising SOC ($\lambda = 0$), it is possible to solve the spectrum analytically:

$$E^2 = E_t^2 + E_R^2 + V_Z^2 + \Delta^2 \pm 2\sqrt{E_t^2(E_R^2 + V_Z^2) + V_Z^2\Delta^2}, \tag{5}$$

where $E_R^2 = E_{R_x}^2 + E_{R_y}^2$. The relevant subgap physics is described by $\pm E_-(k)$, where $E_-(k)$ is the square root of $E^2(k)$ corresponding to the negative sign in Eq. (5). The Ising SOC vanishes on reflection symmetric line $\Gamma - M$, so the above result holds there even when the Ising SOC is present.

2. TOPOLOGICAL PROPERTIES

In-plane Rashba SOC, perpendicular Zeeman field and s-wave pairing have been identified as the building blocks for chiral topological superconductivity[2,3]. The standard picture of topological superconductivity in the case of a single parabolic band in the continuum limit is illustrated in Fig. 1b,c in the main text. However, there are a number of novel features that are specific to our system which are not present in the standard picture. For example, as shown below, the lattice model naturally realizes topological phases classified by larger Chern numbers $|C| > 1$. Chern numbers are integer-valued invariants that classify distinct topological phases in 2D superconductors with broken time-reversal symmetry. In a finite system, the absolute value $|C|$ gives the number of chiral Majorana modes circulating around a boundary between topologically trivial and non-trivial phases. The topological response of the system corresponds to a quantized thermal conductance which has not been measured with a sufficient precision in superconducting systems. However, a nontrivial topology implies that even systems with irregular edges (which do not support accidental edge states) should exhibit topologically protected edge modes. This provides a clear signature of the topological superconductivity.

The distinct topological phases are separated by gap closing transitions. This provides a practical method to calculate the topological phase diagram. Since the spectrum, eq. (5), is symmetric with respect to positive and negative energies, the gap closing transitions can be solved from condition $E_-(k) = 0$ (in the absence of Ising SOC). The gap closing is only possible when the Rashba SOC vanishes, corresponding to Γ, M, M', K and K' points of a hexagonal Brillouin zone (BZ). In these points the gap closing condition yields a relation

$$E_t^2 + V_Z^2 + \Delta^2 - 2|V_Z|\sqrt{E_t^2 + \Delta^2} = 0, \tag{6}$$

which has a solution $|V_Z| = \sqrt{E_t^2 + \Delta^2}$. In the studied experimental system, the magnetic splitting and superconducting scales are well separated, $|V_Z|/\Delta \sim 100$ so the gap closing condition essentially becomes $|E_t| = |\epsilon(k_0) - \mu| = \sqrt{V_Z^2 - \Delta^2} \approx |V_Z|$, where k_0 stands for either Γ, M (M') or K (K'). Since the Ising SOC must also vanish in time-reversal invariant points Γ and M, the gap closing condition (6) remains valid there. However, at K and K' points the gap closings are affected by finite Ising SOC.

Now that we have identified the gap closing transitions, it remains to identify the topological phases and Chern numbers in each of the gapped states. Since the presence of

the magnetic island leads to an a priori unknown renormalization of the effective chemical potential, we will study the phase diagram as a function μ. In Fig. 3b in the main text we have plotted the energy gap diagram as a function of $\epsilon(k) - \mu$ and the Zeeman splitting. This clearly shows the cap closing transitions and opening of topological phases when $|\epsilon(k_0) - \mu| \leq \sqrt{V_Z^2 - \Delta^2}$ is satisfied. The corresponding Chern numbers (evaluated by standard methods) are $C = -1$ (for $k_0 = \Gamma$), $C = -2$ (for k_0 =K, K') and $C = 3$ (for k_0 =M, M'). The energy onset of $C = -1$ phase in Fig. 3b is exaggerated since the 3rd neighbour tight-binding approximation starts to deviate from the real band structure at the top of the band. However, as discussed below, the details at high energies $E \gtrsim 0.5$ eV near the top of the band are irrelevant for interpretation of the experimental results.

In Supplementary Fig. 2 we display the spectra of a semi-infinite strip with a finite width in each of the topologically nontrivial phases, showing exactly $|C|$ edge modes traversing the bulk gap. These results are insensitive of the specific details of the band structure. The result for the $C = 3$ case corresponds to Fig. 2d in the main text. The absolute values of Chern numbers have a simple interpretation due to the crystal symmetry. The first BZ is hexagonal, with the Γ point in the center, while different M and K points (and their time-reversed partners) are located on the boundaries. The band structure around these points gives rise to a Berry flux with unit integrated topological charge. Since the Γ point is fully contained in the BZ, the resulting topological phase has a unit Chern number. Both M and K points and their time-reversed counterparts have multiplicity three in the first BZ. Since the K and K' points each contribute equally but contain only 1/3 of the Berry flux in the first BZ, they collectively give rise to a topological charge $6 \times \frac{1}{3} = 2$. Similarly, M points each contribute equally, but half of their Berry flux is contained in the first BZ. Thus the gap closing transition at M points results in a Chern number $6 \times \frac{1}{2} = 3$.

The obvious candidate state, consistent with the experimental signatures, is the topological $C = 3$ state resulting from the gap closing transition at the M point, where in an isolated $NbSe_2$ there is a band crossing due to Kramers degeneracy about $\lesssim 200$ meV below the Fermi level. The ab initio calculations suggest that proximity to the magnetic $CrBr_3$ island can open up a sizable Zeeman gap of the order of $\lesssim 100$ meV between the Kramers partners at M point. This provides relatively large topological region for the chemical potential where condition $|\epsilon(k_0) - \mu| \leq |V_Z|$ is satisfied. To reach the topological phase, the chemical potential should be shifted down by $\sim 100 - 200$ meV in the region under the

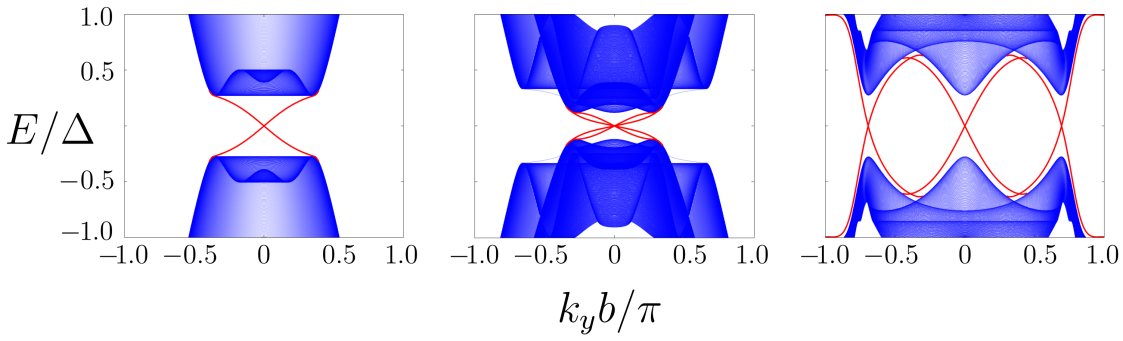

Supplementary Figure 2. The spectrum of a semi-infinite strip ($b = \sqrt{3}$) for topological phases $C = -1$, $C = -2$ and $C = 3$. The hopping parameters are $t_1 = 40$ meV, $t_2 = 132$ meV, $t_3 = 12$ meV and the chemical potentials $\mu = 1.08$ eV, 0.64 eV and -0.26 eV respectively. We have employed exaggerated values $\Delta = 0.1$ eV, $V_Z = \alpha_R = 0.2$ eV, which do not affect the qualitative subgap structure.

magnetic island. A local shift in the effective chemical potential is indeed expected due the scalar potential contribution of the magnetic island. Since the expected Zeeman gap and the required shift are of the same order, this does not require any fine tuning of system parameters. On the other hand, to reach the other two topological regions, the chemical potential shift should be of the order of the relevant d-orbital band width (0.6 eV). This makes them highly unlikely to be realized in the experimental setup.

The energy gap protecting the topological state can be estimated with the help of the distance to the closest Zeeman split band at the M point and the pairing gap opened up at the (shifted) Fermi surface. The energy gap of the topological state is the smaller of these quantities. Since the typical energy scale of Zeeman splitting in the system is two orders of magnitude larger than Δ, the pairing gap at the Fermi level determines the topological gap (assuming that the Fermi energy is not fine tuned to a Zeeman-split band edge). In the parabolic model with Rashba and Zeeman couplings, the magnitude of the topological gap opening at the Fermi surface is estimated by $\Delta_t = \frac{E_R}{\sqrt{E_Z^2+E_R^2}}\Delta$, where E_R and E_Z are the characteristic Rashba and Zeeman energy scales at the Fermi level in the normal state[4]. This result also serves as an order-of-magnitude estimate for the gap in our model as illustrated in Fig. 2c in the main text. The estimate for the gap shows that even though the Zeeman energy is much larger than Δ, the superconducting pairing remains effective due to the

Rashba coupling. Since the experimentally observed Δ_t is a significant fraction of Δ, we can immediately deduce that the Rashba energy scale should be of the order of E_M. Near the M point, ab initio calculations give an estimate $E_M \lesssim 100$ meV. Thus, in the experimental system we have a hierarchy of energy scales $E_R \sim E_Z \sim 100\Delta$.

The effects of Ising SOC are adversarial to the gapped phases discussed above. In the presence of perpendicular magnetization and the Rashba coupling, the Ising SOC in general drives the system towards a gapless phase, lifting the topological protection of the bulk and the edge states. The Ising energy scale should be much smaller than Δ for the gapped states to persist in the studied system. In a monolayer $NbSe_2$, the maximal Ising splitting can reach ~ 100 meV near the K point, giving rise to robust superconductivity for large in-plane magnetic fields[5]. In contrast, for bulk 2H-$NbSe_2$ the Ising splitting for the quasi-2D band for vanishing perpendicular momentum $k_z = 0$ near M point is negligible compared to the monolayer value[6]. Experimentally, the fact that we observe a clear signatures of a spectral gap and edge modes provides strong support that the Ising SOC does not play a role in the studied system.

3. SIMULATING EXPERIMENTAL SIGNATURES

The observation of signatures from the edge modes provides a direct link between the theory and experiments. The hallmark of topological edge modes are their existence for a finite subgap energy interval for all samples, including the ones with irregularly geometry. These features were observed in experiments and here we outline how these features arise from our model. In particular, we investigate irregular geometries analogous to those studied in the experiment and show that the subgap LDOS from the topological edge modes exhibit similar spatially inhomogeneous structure.

The simulation of the LDOS is complicated because of the large separation of the energy scales. The relevant bandwidth (0.6 eV) is nearly three orders of magnitude larger than the superconducting gap $\Delta \sim 1$ meV. To reach an energy resolution which can distinguish details within resolution of a few percent of Δ, the linear dimension of the computational lattice should be of the order 1000-10000 sites. Considering also the large number of eigenstates needed to cover the whole energy region of interest on large lattices, the diagonalization becomes computationally complex even with optimized sparse matrix algorithms. The com-

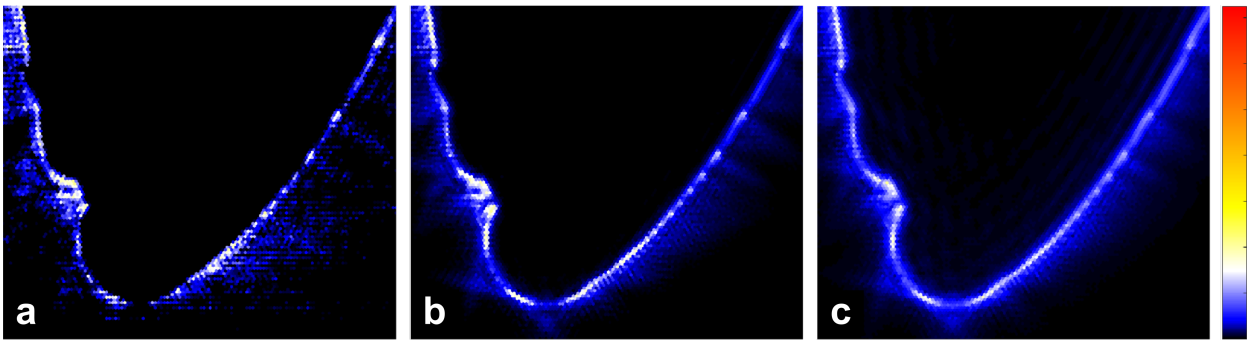

Supplementary Figure 3. **a-c,** Midgap LDOS maps ($E = 0$) for different values Δ: (a) corresponds to physical value $\Delta = 1.25$ meV while (b) and (c) correspond to exaggerated values $\Delta = 10$ meV and $\Delta = 20$ meV, respectively. The parameters are $t_1 = 40$ meV, $t_2 = 132$ meV, $t_3 = 12$ meV, $\alpha_R = 60$ meV and chemical potential in the bulk was $\mu_B = -111.2$ meV. Chemical potential and the Zeeman splitting on the island was $\mu_I = -260$ meV and the $V_Z = 85$ meV. The calculation has been carried out on a lattice with 10^5 sites.

mon solution to circumvent this is to employ exaggerated values of Δ and to assess the reliability of such approach by studying Δ scaling of the results. Indeed, we have checked in large scale simulations that our calculations performed with exaggerated Δ do faithfully represent the results with realistic small value of Δ. This is demonstrated in Supplementary Fig. 3. Despite the cruder energy resolution of the realistic Δ result, it is clearly established that the essential features of the edge modes, especially the effective penetration depth, are unchanged in the exaggerated Δ calculations and correspond excellently to the experimental observations. This counterintuitive fact is actually completely in line with similar observation in 1d magnetic chains: the edge mode penetration depth is largely insensitive to the bulk value of Δ (not proportional to $1/\Delta$ as naively expected)[7]. This conclusion, reproduced by our 2d model, explains why the penetration depth of the edge modes in topological 1d chains is much smaller than naive expectations. Our theory predicts that the width of the bright edge strip is 5-10 lattice points in excellent agreement with observations. We have also checked that, similarly to $E = 0$ case presented in Fig. 3, the low-energy LDOS features corresponding to realistic value of Δ at higher energies are also accurately reproduced by scaled up Δ calculations when expressed in the units of Δ. This facilitates a convenient exploration of the full energy window of interest.

To simulate $\mathrm{d}I/\mathrm{d}V$ maps obtained by the STM we numerically solve the tight-binding

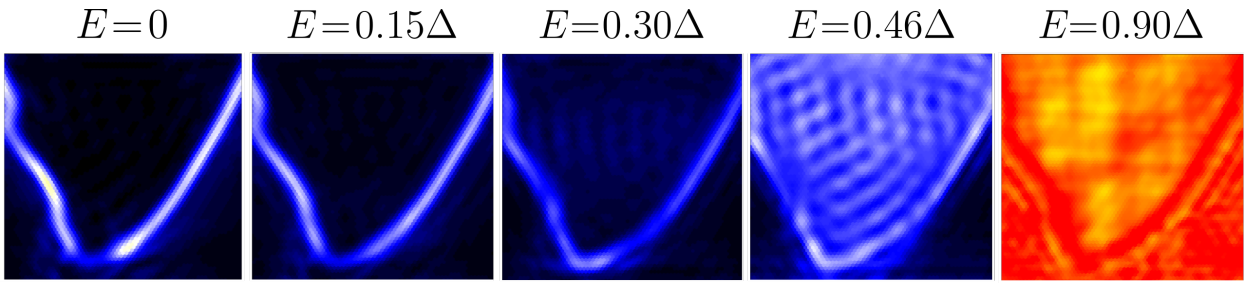

Supplementary Figure 4. Theoretical calculation of LDOS maps. The parameters are $t_1 = 40$ meV, $t_2 = 132$ meV, $t_3 = 12$ meV, $\alpha_R = 60$ meV and chemical potential in the bulk was $\mu_B = -111.2$ meV. Chemical potential and the Zeeman splitting on the island was $\mu_I = -260$ meV and the $V_Z = 85$ meV. We have employed scaled-up value $\Delta = 20$ meV.

Hamiltonian Eq. 1 on a 95×96 triangular lattice with periodic boundary conditions. By putting the Zeeman splitting terms in appropriate sites we define the shape of the island which mimics the one grown by MBE (smooth edge on the right and an irregular one on the left). The effects we describe are generic and do not depend on the exact shape of the island. To avoid a sharp discontinuity in both magnetic field and chemical potential, we assume that every impurity atom influences its surroundings so that the effective potential felt by every site of the lattice becomes $V_{\alpha i} = \sum_j V_{0\alpha i} exp(-r_{ij}/l)$, where $\alpha = Z, S$. $V_{0\alpha}$ is the potential contribution of the impurity site and r_{ij} is the distance of i-th lattice site from the j-th impurity site. As the outcome of this procedure, the Zeeman field of the island region is $V_Z \simeq 85$ meV and decreases to zero over a few lattice sites (we set the length of the decay $l = 2.2a$, with a the lattice constant). The effective shift of the chemical potential induced by the island is about -155 meV (with respect to the pristine $NbSe_2$ bulk value supplied by the DFT calculations) and the Rashba constant $\alpha_R = 60$ meV. The topological gap is comparable to the experimental value $\Delta_T \sim 0.3\Delta$. As discussed above, a realistic value of the superconducting gap Δ can be faithfully approximated by scaled up value $\Delta = 20$ meV to simulate the experimental findings. As with the STM data, we normalize our results to the normal state LDOS. In Supplementary Fig. 4 we have plotted LDOS for an irregular magnetic island and illustrated its evolution as a function of energy. The subgap LDOS is concentrated on the edges as expected. The regular edge segments show a homogeneous LDOS pattern while the irregularities give rise to enhanced and suppressed parts. This effect, combined with the finite experimental resolution, would

give the impression of "cutoff" edge modes while in reality the edge mode exists everywhere. For energies approaching the topological gap, the LDOS features begin to penetrate to the center of the island. For energies above the topological gap the states are homogeneously distributed in the bulk. More simulation results and their comparison to the experimental data is presented in Supplementary Fig. 5, showing excellent agreement of the main features.

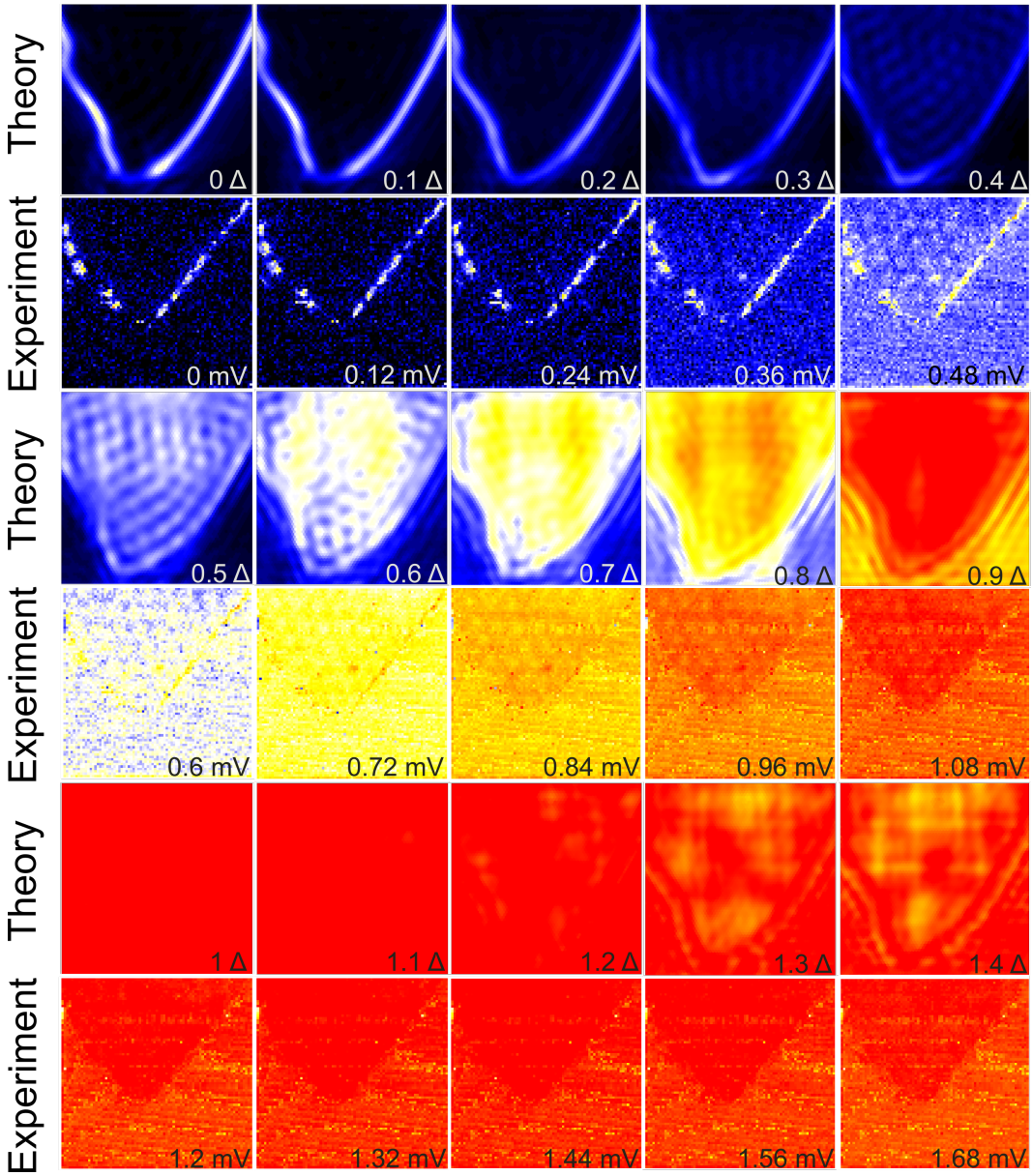

Supplementary Figure 5. Evolution of the edge states with increasing energy. Experimentally measured differential tunneling conductance maps and the corresponding theoretically computed spatially resolved LDOS for the same energies as the experimental results.

In Fig. 3h of the main text we have plotted the calculated LDOS along a line crossing the magnetic island. To produce continuous curves as a function of energy, we have applied a gaussian broadening of 0.1Δ to the spectral lines. The calculated features are in excellent qualitative agreement with the corresponding experimental data. To summarize this section, we note that in addition to the universal features of topological superconductors, our theoretical model predicts important system-specific characteristics in excellent agreement with experimental findings. These include 1) the penetration depth of the edge modes (which is much smaller than naive expectations) 2) The energy-dependence of the subgap LDOS features which stems from the system-specific dispersion of the edge modes (Fig. 3 in the main text) 3) The non-generic coexistence of the edge modes and bulk states above the topological gap (seen in Supplementary Fig. 2c) and in comparison to experiment in Supplementary Fig. 5). These features together provide extraordinary evidence for our conclusions.

---

* Email: kezilebieke.shawulienu@aalto.fi, teemu.ojanen@tuni.fi, peter.liljeroth@aalto.fi

[1] Gerbold C. Ménard, Sébastien Guissart, Christophe Brun, Stéphane Pons, Vasily S. Stolyarov, François Debontridder, Matthieu V. Leclerc, Etienne Janod, Laurent Cario, Dimitri Roditchev, Pascal Simon, and Tristan Cren, "Coherent long-range magnetic bound states in a superconductor," Nat. Phys. **11**, 1013–1016 (2015).

[2] Masatoshi Sato and Yoichi Ando, "Topological superconductors: a review," Rep. Prog. Phys. **80**, 076501 (2017).

[3] Jay D. Sau, Roman M. Lutchyn, Sumanta Tewari, and S. Das Sarma, "Generic new platform for topological quantum computation using semiconductor heterostructures," Phys. Rev. Lett. **104**, 040502 (2010).

[4] Jason Alicea, "Majorana fermions in a tunable semiconductor device," Phys. Rev. B **81**, 125318 (2010).

[5] Xiaoxiang Xi, Zefang Wang, Weiwei Zhao, Ju-Hyun Park, Kam Tuen Law, Helmuth Berger, László Forró, Jie Shan, and Kin Fai Mak, "Ising pairing in superconducting $NbSe_2$ atomic layers," Nat. Phys. **12**, 139–143 (2016).

[6] L. Bawden, S. P. Cooil, F. Mazzola, J. M. Riley, L. J. Collins-McIntyre, V. Sunko, K. W. B.

Hunvik, M. Leandersson, C. M. Polley, T. Balasubramanian, T. K. Kim, M. Hoesch, J. W. Wells, G. Balakrishnan, M. S. Bahramy, and P. D. C. King, "Spin-valley locking in the normal state of a transition-metal dichalcogenide superconductor," Nat. Commun. **7**, 11711 (2016).

[7] Yang Peng, Falko Pientka, Leonid I. Glazman, and Felix von Oppen, "Strong localization of Majorana end states in chains of magnetic adatoms," Phys. Rev. Lett. **114**, 106801 (2015).